KDM2B regulates stroke injury by modulating OGT-mediated 0-GlcNAcylation of SLC7A11

Check for updates

Yi Li[1,4], Liangbo Niu[2,4], Dai Zheng[1,4], Xinxing Zhang[3] ✉, Lu Feng [2] ✉ & Jing Fu [1] ✉

Ischemic stroke poses a significant global health risk. Currently, recanalization of blood flow through surgery or medication is the only effective means to control ischemia-reperfusion injury. This study aims to explore the role and molecular mechanism of OGT in regulating neuronal injury and motor deficits following a stroke. The MCAO and OGD/R models were established to validate the therapeutic efficacy of OGT in mitigating neuronal injury and motor dysfunction following stroke. Molecular biological techniques were employed to assess ferroptosis levels, OGT ubiquitination, and SLC7A11 O-GlcNAcylation. OGT has a therapeutic effect on motor deficits and neuronal damage after stroke by regulating SLC7A11 O-GlcNacylation-mediated ferroptosis, while the KDM2B-mediated ubiquitination pathway is responsible for changes in OGT levels. These findings are crucial for target selection and biomarker identification in stroke treatment.

Stroke, a prevalent and frequently occurring disease of the nervous system, is characterized by high morbidity, disability rate, and mortality worldwide. There are two types of stroke: hemorrhagic stroke and ischemic stroke, with the latter being the most common (accounting for approximately 85%)[1]. Currently, available treatments for ischemic stroke include thrombolytic therapy, anticoagulant therapy, and antiplatelet therapy[1]. Recent studies have shed light on the mechanisms underlying secondary injury after stroke; nerve cell damage is a major contributor to serious harm to the body[2]. Traditional pathways leading to nerve cell damage after stroke include apoptosis, autophagy, oxidative stress, etc., but inhibiting these pathways alone may not be sufficient to fully restore damaged brain tissue or nerve cells[3,4]. Therefore, it is suggested that there might be other ways in which nerve cells die following a stroke.

Ferroptosis is a novel form of cell death that relies on lipid peroxidation, distinguishing it from apoptosis and autophagy[5]. Given the iron-dependent accumulation of lipid peroxides, investigating the interplay between iron and lipid peroxides in this process becomes crucial[6]. Iron plays an indispensable role in maintaining environmental stability and physiological functions within the body, being widely distributed in brain tissue where it serves important functions such as oxygen transport, ATP synthesis, and DNA synthesis. In mice, cerebral ischemia was induced by occluding the right middle cerebral artery and the right common carotid artery for 1 h[5]. Consequently, a significant increase in iron (Fe^{2+}) content (iron overload) was observed in the cerebral cortex, accompanied by a notable reduction in

antioxidant activities of superoxide dismutase and catalase caused by ischemia. Similar findings were reported by Park et al. and Ding et al.[5,7]. However, it has been demonstrated that the administration of iron chelators, free radical scavengers, or antioxidants effectively prevents such damage, providing robust evidence to support these experiments. In conclusion, during ischemic stroke occurrence, diminished levels of antioxidant factors (e.g., glutathione (GSH) and Glutathione Peroxidase 4 (GPX4)) within nerve cells along with accumulation of lipid hydroperoxide (LPO) content in ischemic brain tissue accelerate toxic reactions to nerve cells and exacerbate brain tissue damage[8–10]. Multiple lines of evidence have consistently highlighted the crucial role of ferroptosis in subsequent stroke progression; therefore, inhibiting ferroptosis represents an effective approach to mitigate neurological damage and improve prognosis for post-stroke sequelae[8–10].

Ferroptosis is closely associated with amino acid metabolism and regulates the antioxidant system of amino acids through the System XC- axis[11]. System Xc- is a specific antiporter protein located on the cell membrane surface between glutathione and cysteine. XCT (SLC7A11) and SLC3A2 are linked by disulfide bonds[6,12]. This transport channel simultaneously imports cystine while exporting glutamate. By taking advantage of high concentration differences without requiring ATP energy input, this transport channel is susceptible to inhibition by external high concentrations of valley rock compounds. Research evidence indicates that brain tissue damage following ischemic stroke increases extracellular glutamate levels which directly inhibit

[1]Department of Emergency Medicine, Sichuan Provincial People's Hospital, University of Electronic Science and Technology of China, Chengdu, Sichuan, China. [2]Department of Emergency Surgery, Sichuan Provincial People's Hospital, University of Electronic Science and Technology of China, Chengdu, Sichuan, China. [3]Department of Geriatric, Sichuan Provincial People's Hospital, University of Electronic Science and Technology of China, Chengdu, Sichuan, China. [4]These authors contributed equally: Yi Li, Liangbo Niu, Dai Zheng. ✉e-mail: zhangxinxing1979@163.com; feenglu1974@sina.com; 2220137@uestc.edu.cn

cysteine absorption. After cellular entry, cysteine undergoes a series of catalytic reactions and is rapidly reduced to caspases, which are ultimately synthesized into GSH through the intricate processes of caspase-glutamine synthesis, glutathione-semicitromalondialdehyde synthesis, and ATP metabolism[13]. Consequently, we infer that modulation of any component within the System Xc- axis can directly or indirectly regulate mobile GPX4 activity and effectively impact ferroptosis progression, thereby identifying potential therapeutic targets for stroke[14].

O-GlcNAcylation is a specific form of glycosylation modification that involves the attachment of N-acetylglucosamine (GlcNAc) to the hydroxyl group of serine (Ser) or threonine (Thr) residues in proteins through an O-glycosidic bond. This post-translational modification is widely distributed within cells and primarily governs protein functionality, stability, as well as intracellular metabolism and signaling pathways[15]. This monosaccharide alteration has been identified as a pivotal regulator in numerous vital biological and pathological processes, including signal transduction, protein interactions, and enzyme activity[16]. Unlike most other PTMs (post-translational modifications), O-GlcNAc acylation is catalyzed by only two conserved enzymes: O-GlcNAc transferase (OGT) and O-GlcNAcase (OGA), which mediate the addition and removal of O-GlcNAc groups respectively[16]. Previous studies have demonstrated that aberrant O-GlcNAcylation is associated with malignant properties in cancer cells. A recent study revealed that inhibition of O-GlcNAcylation leads to mitochondrial fragmentation while enhancing mitophagy, thereby providing an additional source of labile iron and rendering cells more susceptible to ferroptosis. Although some studies suggest that targeting OGT may hold promise for stroke treatment, reliable data validating its therapeutic value are still lacking; furthermore, no comprehensive investigations have explored its underlying mechanism[16–19].

In summary, the present study aims to establish an OGT intervention model in order to validate its therapeutic efficacy on neuronal injury in vivo model of ischemia-reperfusion and gain further insights into its altered expression and molecular mechanism from the perspective of ferroptosis. This investigation will provide a crucial foundation for selecting targets for targeted stroke therapy.

Result

Therapeutic effect of OGT overexpression in a mice model of MCAO

To further investigate the regulatory role of OGT in the MCAO model, we initially established an OGT overexpression model (Supplementary Fig. 1). Subsequently, employing the TTC staining technique, we observed a significant augmentation in the area of ischemic injury in the MCAO group compared to the Sham group. However, it is encouraging to note that overexpression of OGT led to a substantial reduction in the ischemic area (Fig. 1A, B). In order to comprehensively evaluate the impact of OGT overexpression on brain injury, we additionally employed nerve injury scoring and brain edema assessment methods. The results demonstrated that OGT overexpression significantly ameliorated neurological damage and brain edema induced by MCAO (Fig. 1C, D). Considering NeuN and PSD95's pivotal role in assessing neuronal functional impairment, their expression was specifically examined. The expression levels of these two crucial markers were markedly restored in the OGT overexpression group compared with the MCAO group, further confirming OGT's important neuroprotective role (Fig. 1E). Furthermore, behavioral improvement resulting from OGT was also observed through Open field testing and rotarod testing (Fig. 1F). To visually demonstrate tissue damage more intuitively, HE and Nissl staining were utilized for brain tissue staining purposes. The findings revealed a significant ischemic area along with neuronal damage and reduced neuron count within the MCAO group; however, these effects were substantially reversed by OGT overexpression (Fig. 1G). Collectively, these data strongly indicate that OGT overexpression can effectively restore neuronal damage caused by MCAO.

Role of ferroptosis in amelioration of neuronal injury induced by ischemia-reperfusion by OGT

To investigate the specific role of OGT in neuronal injury, we constructed an OGD/R model and an OGT overexpression model using HT-22 cells. Our results demonstrate that overexpression of OGT could reverse cell death induced by OGD/R, as evidenced by CCK-8 and EDU staining (Fig. 2A, B). CytoTox-Glo cytotoxicity assays showed that OGT overexpression reversed OGD/R-induced cell death in HT-22 cells (Fig. 2C). Furthermore, examination of NeuN and PSD95 protein expression revealed that OGT could restore the decreased expression caused by ischemia-reperfusion (Fig. 2D). These findings provide further support for our in vivo results and confirm the ability of OGT to mitigate neuronal damage.

To further investigate the neuroprotective effects of OGT, we downloaded the GSE196266 dataset from GEO and divided it into high and low-expression groups based on median OGT expression. A heatmap was generated to visually compare the top 10 upregulated genes in each group (Supplementary Fig. 2A). Gene enrichment analysis revealed significant enrichment of ubiquitination activity and aminoacyltransferase activity among differentially expressed genes, providing insight into the mechanisms underlying OGT action (Supplementary Fig. 2B). Additionally, KEGG analysis identified involvement of cystine/glutamate metabolic pathway and lipid metabolic pathway in regulating neuronal injury (Supplementary Fig. 2C). Given the crucial role of lipid metabolism in stroke-induced neuronal death, particularly its association with ferroptosis regulation, this finding provides a valuable direction for future research.

Based on the aforementioned bioinformatics analysis, we conducted a systematic examination of the oxidative damage indicators in our model. The results revealed a significant increase in levels of oxidative damage products ROS and MDA in the OGD/R model, which were effectively reversed by overexpression of OGT (Fig. 2E–G). Furthermore, restoration of GSH content was observed in the OGT overexpression group, providing further confirmation of the beneficial role played by OGT in protecting against oxidative damage (Fig. 2F). To visually depict the impact of OGT overexpression on ROS and Fe^{2+}, fluorescence labeling using DCFH-DA and Ferrogange was employed. Remarkably, OGT overexpression exhibited substantial inhibition of ROS and Fe^{2+} elevation (Fig. 2H, I). Additionally, expression levels of SOD and GSH were examined in both brain tissues from an in vivo model as well as HT-22 cells from an in vitro model, yielding consistent results with our bioinformatics data. Notably, ROS content was significantly suppressed within the OGT overexpression group, thereby further corroborating our findings (Fig. 2J). In order to confirm the regulatory effect of OGT on ferroptosis, we used RSL3 (ferroptosis inducer) combined with OGT overexpression and inhibition groups for IC50 detection and found that overexpression of OGT reduced ferroptosis sensitivity while si-OGT enhanced ferroptosis sensitivity (Supplementary Fig. 3). Collectively, these outcomes strongly suggest that modulation of ferroptosis pathway may underlie neuronal damage amelioration mediated by OGT; thus offering novel directions for future research.

Regulation of inflammatory responses in microglia by OGT

Recent studies have demonstrated the impact of ferroptosis on the inflammatory response following stroke. Our previous findings substantiate that OGT can mitigate post-stroke neuronal damage by inhibiting ferroptosis levels. Additionally, IHC staining revealed that OGT overexpression suppressed Iba1 expression in mouse brain microglia (Fig. 3A). Subsequent staining of CD86 and CD206-labeled microglia indicated a significant inhibition of CD86 expression induced by MCAO with OGT overexpression, while CD206 expression was significantly increased (Fig. 3B). To further investigate the inflammatory factors in brain tissue, we assessed the expression of pro-inflammatory cytokines IL-1α and TNF-α in MCAO mice brains and observed that OGT overexpression attenuated the inflammatory response (Fig. 3C). Conversely, OGT also promoted the production of anti-inflammatory cytokines (IL-4 and IL-10) (Fig. 3D). In
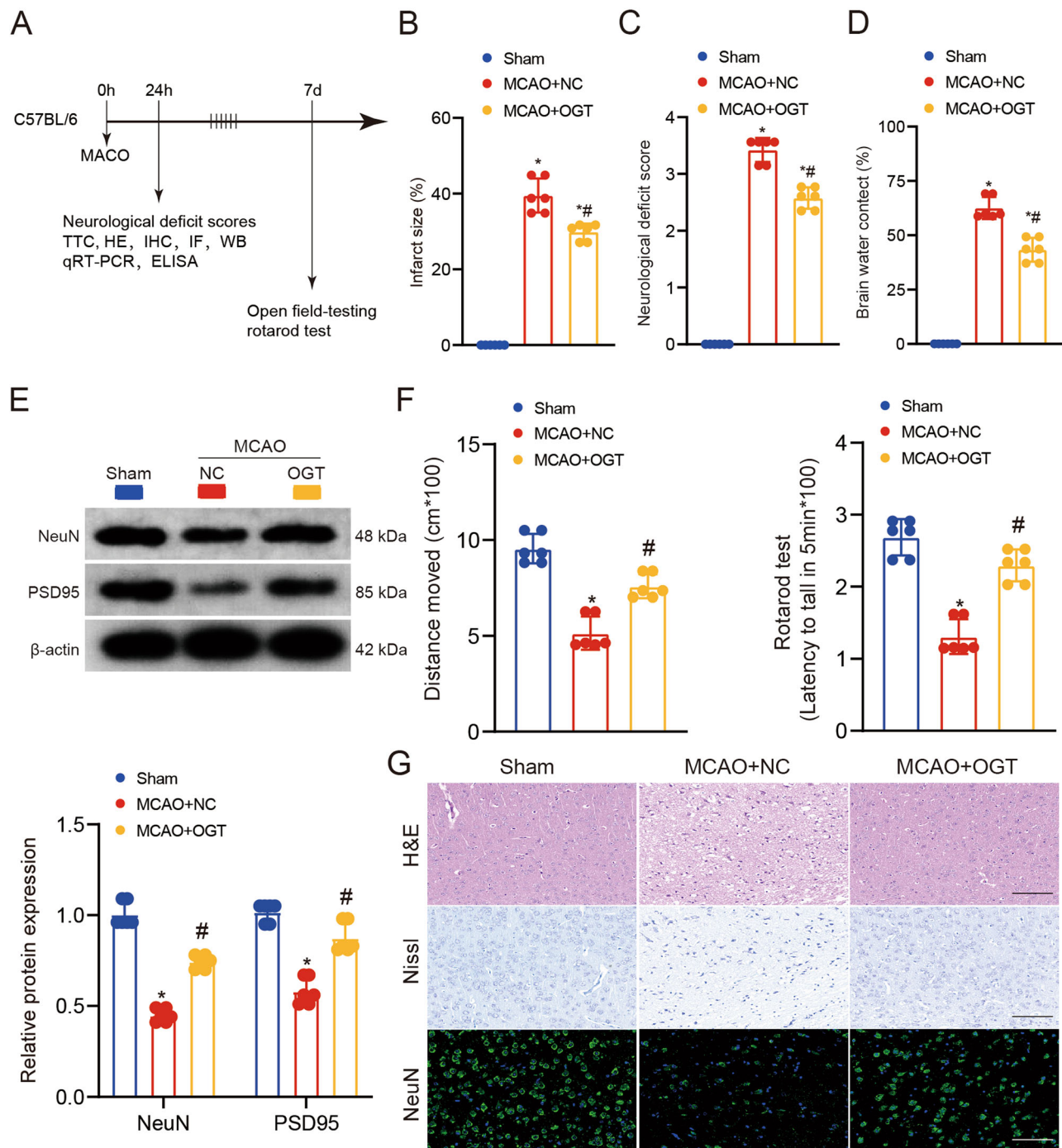
Fig. 1 | Therapeutic effect of OGT overexpression in a mice model of MCAO.
MCAO model mice overexpressing OGT were constructed. **A** A diagram of the animal processing flow. **B** TTC staining reveals the ischemic area in different experimental groups, $n = 6$. **C** Nerve injury scores were assessed in different experimental groups, $n = 6$. **D** Brain water content was measured in different experimental groups, $n = 6$. **E** Protein expression levels of NeuN and PSD95 were analyzed using Western blotting in different experimental groups, $n = 6$. **F** The open field-testing and rotary-rod tests were conducted on mice from different experimental group, $n = 6$. **G** HE, Nissl, and NeuN IHC staining techniques were employed to examine rat brain samples from various experimental groups (scale bar = 100 μm). Results are presented as group mean ± standard deviation. *$p < 0.05$ vs. Sham group; #$p < 0.05$ vs. MCAO + NC group.

order to gain deeper insights into the mechanism underlying OGT's improvement of inflammatory response, we cultured BV2 cells with HT-22 cell culture medium treated with both OGT and OGD/R. The results showed that the group with OGT overexpression significantly suppressed inflammation while promoting an anti-inflammatory response in BV2 cells (Fig. 3E, F). These data further support our in vivo findings and suggest that understanding how OGT regulates neuronal cells may be crucial for ameliorating stroke.

Role and site of SLC7A11 O-GlcNAcylation in OGT overexpression

Our results show that OGT has a significant effect on cystine uptake in HT-22 cells (Fig. 4A), a finding strongly supported by bioinformatics data (Supplementary Fig. 2C). Given that cystine is mainly imported from the extracellular environment through the cystine/glutamate antiporter system xc- (Fig. 4B), we further investigated whether SLC7A11, a key and functional subunit of this system, is regulated by OGT. The results showed that
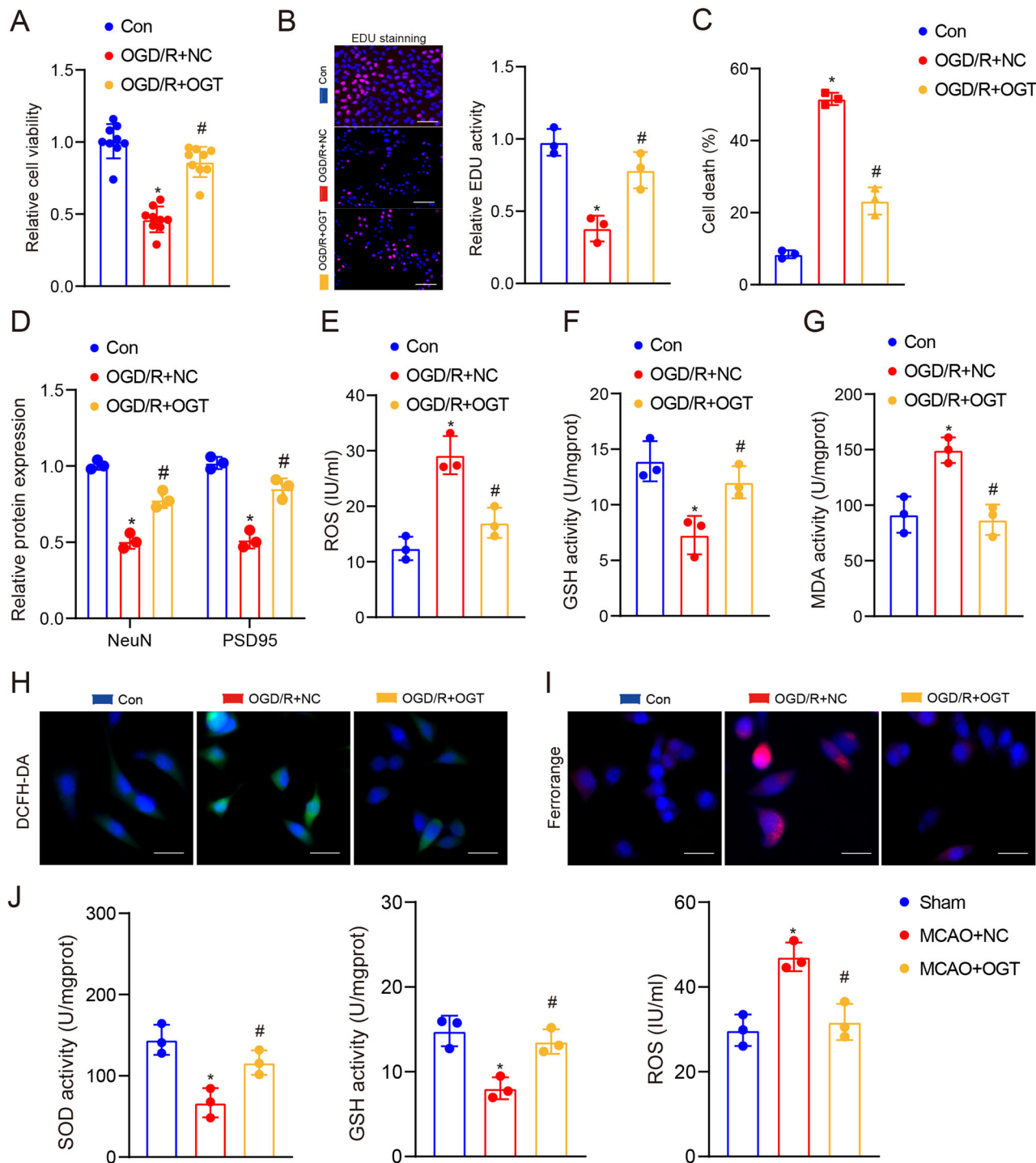
Fig. 2 | Role of ferroptosis in amelioration of neuronal injury induced by ischemia-reperfusion by OGT. Constructed an OGD/R model and an OGT overexpression model using HT-22 cells. **A** CCK-8 assay was used to detect the proliferation of HT-22 cells in different groups. **B** EDU staining was used to detect the proliferation of HT-22 cells in different groups, $n = 3$. **C** CytoTox-Glo cytotoxicity assays were used to detect the cell death rate of each treatment group. **D** Western blotting method was used to detect the protein expression levels of NenN and PSD95. **E–G** ROS, GSH, and MDA contents were measured in different groups of cells. $n = 3$. **H** Fluorescent labeling of ROS in different groups of cells using DCF-HA, $n = 3$. **I** Ferrorange was used for fluorescent labeling of Fe in cells, $n = 3$. Results are expressed as group mean ± standard deviation. *$p < 0.05$ vs. Con group #$p < 0.05$ vs. OGD/R + NC group. **J** Determination of SOD, GSH, and ROS content in brain tissue of the in vivo model. $n = 3$. (scale bar = 20 μm) Results are expressed as group mean ± standard deviation. *$p < 0.05$ vs. Sham group; #$p < 0.05$ vs. MCAO + NC group.

OGT overexpression could significantly restore SLC7A11 expression level (Fig. 4C). Given the properties of OGT as an O-GlcNAc transferase, we hypothesized that O-GlcNAc might be involved in the process of OGT regulating the stability of SLC7A11 protein. To test this hypothesis, we first examined the interaction between OGT and SLC7A11 under physiological conditions using the Co-Ip. Subsequently, we used an anti-O-glcnAc antibody to detect the immunoprecipitated SLC7A11 (Fig. 4D, E). Excitantly, we found that O-GlcNAc modification was indeed present in immunoprecipitated SLC7A11 and that depletion of OGT resulted in reduced O-GlcNAc modification levels of SLC7A11 (Fig. 4F). Furthermore, we
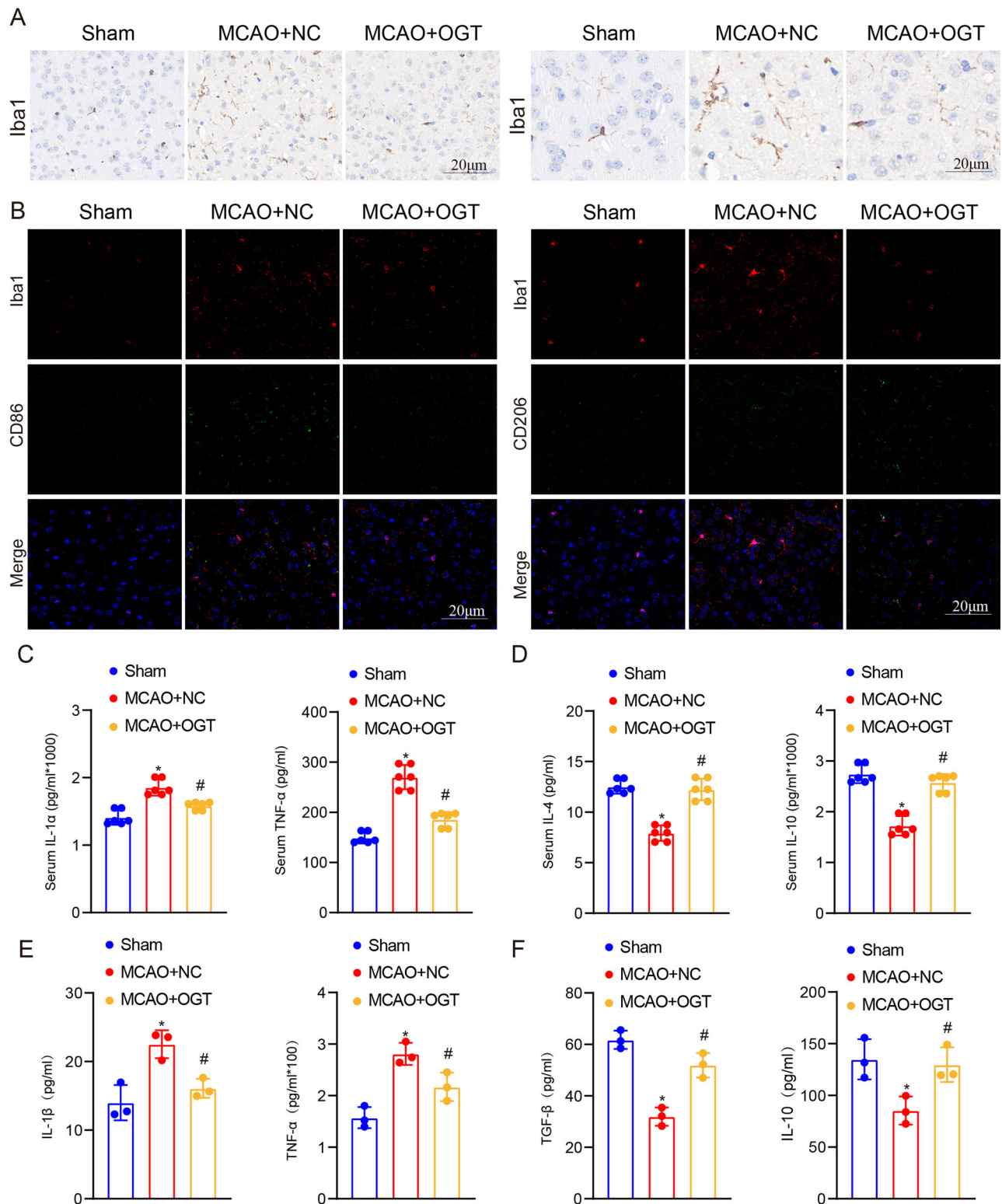
Fig. 3 | Regulation of inflammatory responses in microglia by OGT.
A Immunohistochemical method was used to detect the protein level of Iba1 in brain microglia of MACO mice (scale bar = 20 μm). **B** Immunofluorescence detection of the expression of CD86 and CD206 in the brain of MACO mice (scale bar = 20 μm). **C** ELISA was used to detect the expression of pro-inflammatory cytokines IL-1α and THF-α in the brain tissue of MACO mice, $n = 6$. **D** ELISA was used to detect the expression of anti-inflammatory cytokines IL-4 and IL-10 in the brain tissue of

MACO mice, $n = 6$. Results are expressed as group mean ± standard deviation. *$p < 0.05$ vs. Sham group; #$p < 0.05$ vs. MCAO + NC group. OGD/R and OGT-treated HT-22 medium were used to culture BV2 cells. **E** The contents of IL-1β and THF-α in the different groups were determined $n = 3$. **F** The contents of TGF-β and IL-10 in the different groups were determined $n = 3$. Results are expressed as group mean ± standard deviation. *$p < 0.05$ vs. Con group #$p < 0.05$ vs. OGD/ R + NC group.

Article

observed increase in the global O-GlcNAc modification level in cells treated with TMG, an OGA inhibitor, which resulted in an increase in the O-GlcNAc modification level of SLC7A11. In contrast, we observed the opposite phenomenon in cells treated with OSMI-1, an OGT inhibitor (Fig. 4G). These results further support our hypothesis that O-GlcNAc modification plays a critical role in OGT regulation of SLC7A11. These
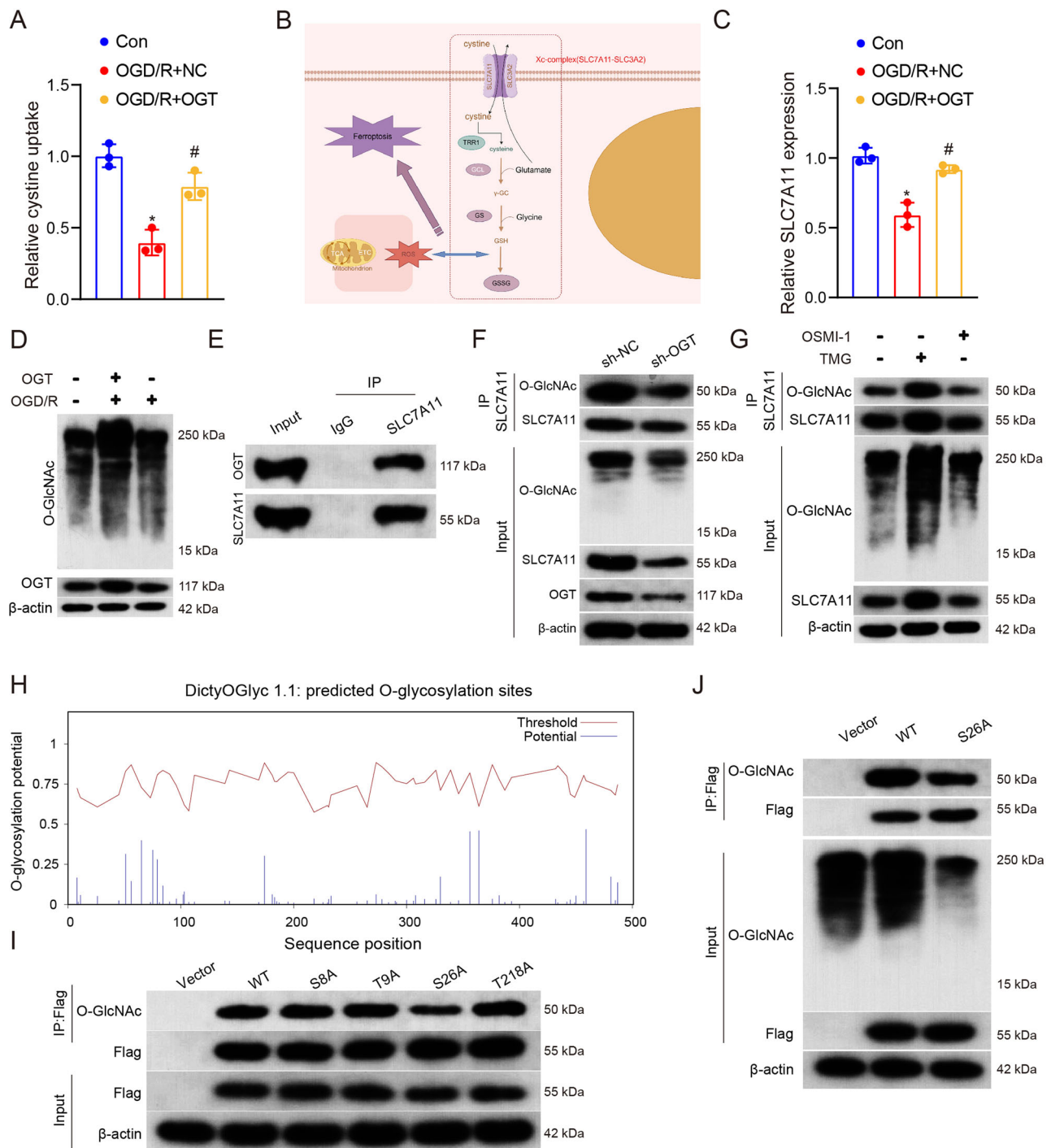
Fig. 4 | Role and site of SLC7A11 O-GlcNAcylation in OGT overexpression.
A Cystine uptake assay in HT-22 cells under OGD/R and OGT treatment. $n = 3$. Results are expressed as group mean ± standard deviation. *$p < 0.05$ vs. Con group #$p < 0.05$ vs. OGD/R + NC group. **B** Mechanistic diagram of the intracellular system xc-. **C** Expression levels of SLC7A11 in HT-22 treated with OGD/R and OGT by qRT-PCR, $n = 3$. Results are expressed as group mean ± standard deviation. *$p < 0.05$ vs. Con group #$p < 0.05$ vs. OGD/R + NC group. **D** WB measurement of O-GlcNAcylation and OGT levels in HT-22 treated with OGD/R and OGT. **E** The Co-IP assay to determine the association of endogenous SLC7A11 and OGT in HT-22 cells. **F** SLC7A11 protein and its O-GlcNAcylation levels were determined by Co-IP. Sh-OGT and sh-NC were transfected into HT-22 cells, and SLC7A11 was

precipitated with anti-SLC7A11 antibody. O-glycosylated SLC7A11 was immuno-precipitated with an anti-O-GlcNAc antibody. **G** HT-22 cells were treated with TMG (10 μM, 24 h) and OSMI-1 (50 μM, 24 h), and the protein levels of SLC7A11 and its O-GlcNAcylation were determined by Co-IP. **H** Map of predicted SLC7A11 O-GlcNAcylation sites by DictyOGlyc 1.1. **I** Alanine mutation at SLC7A11S8, T9, S36, and T218 sites was performed according to the predicted results, and HT-22 cells were transfected with a plasmid expressing the Flag tag. Co-IP was used to measure the O-GlcNAcylation level of SLC7A11. **J** Recombinant plasmids expressing FLAG-tagged SLC7A11 wild-type and SLC7A11-S26A mutant were transfected into HT-22 cells, and the O-O-GlcNAcylation levels of WT and mutant were determined by Co-IP.
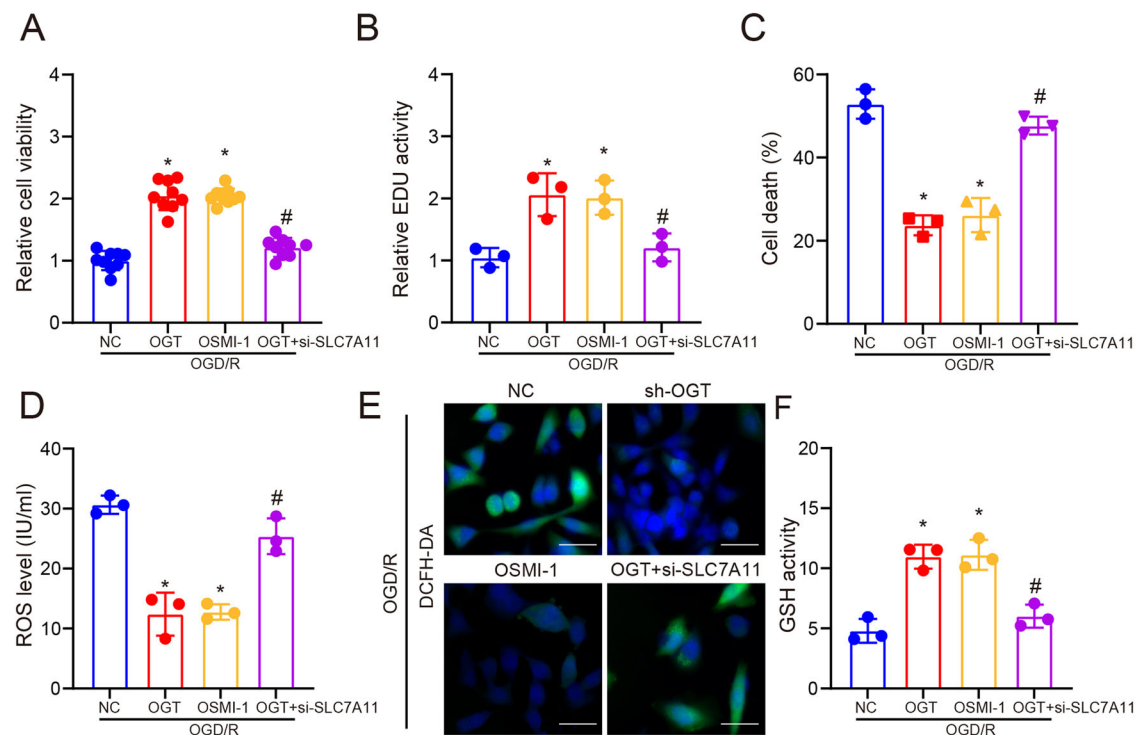
Fig. 5 | OGT regulates neuronal ferroptosis through SLC7A11 to improve HT-22 injury. OGT and si-SCL7A11 were transfected into OGD/ R-induced HT-22 cells or treated with OSMI-1 (50 μM, 24 h) in combination and divided into OGT over-expression group, OSIM1-1 group, and OGT + si-SLC7A11 group. **A** The cell viability of different groups was measured by CCK-8 assay, $n = 3$. **B** EDU staining was used to determine cell proliferation ability in different groups. Scale bar: 20 μM, $n = 3$. **C** CytoTox-Glo cytotoxicity assays were used to detect the cell death rate of each treatment group. **D** ELISA assay was used to detect ROS content in different groups, $n = 3$. **E** Immunofluorescence staining of different groups of ROS using DCFH-DA, scale bar: 20 μM. **F** The activity of GSH in different groups was measured, $n = 3$. Results are expressed as group mean ± standard deviation. $^*p < 0.05$ vs. NC group; $^#p < 0.05$ vs. OGT group.

results suggest that OGD/R is able to modulate O-GlcNAc acylation of SLC7A11 via OGT, which may affect its function and stability.

The potential O-GlcNAc loci in SLC7A11 were initially predicted using bioinformatics tools available online (https://services.healthtech.dtu.dk/) (Fig. 4H). Subsequently, four residues (S8, T9, S26, and T218) were selected for experimental validation. Each of these residues was mutated to alanine individually. Notably, the mutation at residue S26 significantly attenuated the O-GlcNAcylation signal compared to the other three mutations, indicating that S26 serves as the primary O-GlcNAcylation site (Fig. 4I, J).

OGT regulates neuronal ferroptosis through SLC7A11 to improve HT-22 injury

To verify the role of the OGT/SLC7A11 axis in regulating OGD/R-induced HT-22 damage, we constructed the OGT overexpression group, OSMI-1 group, and OGT + si-SLC7A11 group, respectively. In OGD/R-treated HT-22 cells, the addition of si-SLC7A11 reversed the therapeutic effects of OGT and OSMI-1 on HT-22 cell injury using CCK-8, EDU staining and CytoTox-Glo cytotoxicity assays (Fig. 5A–C). Finally, to verify the effect of OGT on ferroptosis, we detected ROS content and ROS level by immunofluorescence and found that OGT could inhibit ferroptosis by affecting O-GlcNAc of SLC7A11 to improve OGD/ R-induced HT-22 cell damage (Fig. 5D–F).
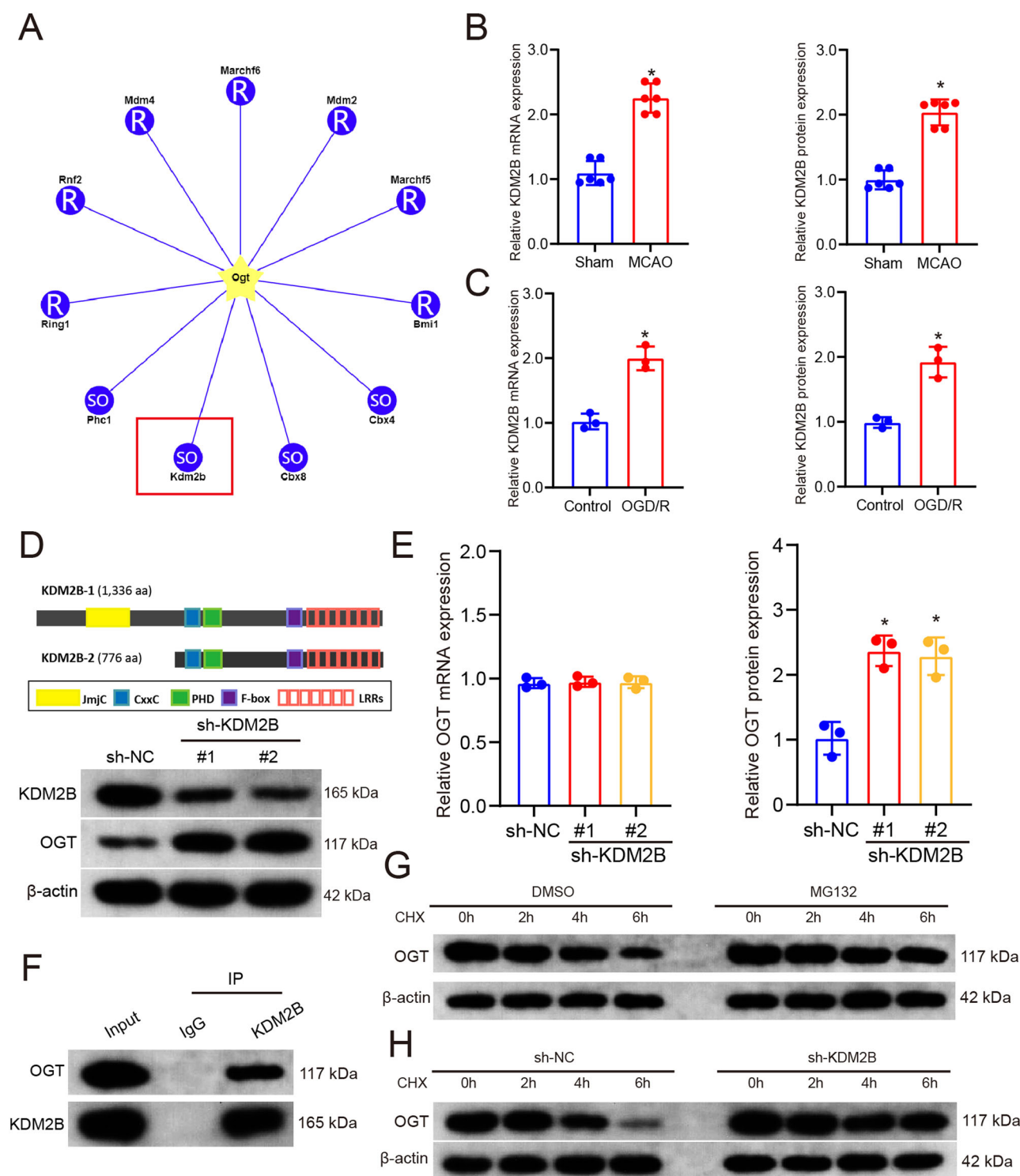
KDM2B may be involved in the regulation of OGT ubiquitination

Interestingly, despite the successful construction of the OGT overexpression model, it is surprising to find that OGT primarily functions at the protein level in the MCAO model (Supplementary Fig. 1). Therefore, in order to comprehensively analyze the underlying cause of OGT changes, we integrated our previous GO analysis results and postulated that ubiquitination

regulation may serve as a fundamental mechanism for OGT alterations following stroke (Supplementary Fig. 2). This mechanism has been extensively supported by numerous studies in stroke research[20,21]. Consequently, we initially predicted potential interactions between OGT and ubiquitin E3 ligases and identified KDM2B as a putative regulator of its ubiquitination process (Fig. 6A). To validate this hypothesis, both KDM2B mRNA and protein expression levels were assessed in both MCAO and OGD/R models (Fig. 6B, C).

KDM2B was a histone demethylase[22–24], so to verify the regulatory mechanism of KDM2B on OGT. We first constructed HEK293 cells with stable knockdown of KDM2B. KDM2B generates multiple isoforms through alternative splicing and differential transcription initiation. KDM2B-1 (NM_032590) is the longest and likely full-length isoform carrying the histone demethylase JmjC domain, whereas KDM2B-2 (NM_013910), translated from an mRNA starting from the internal promoter of the KDM2B-1 transcript, lacks the JmjC domain (Fig. 6D). We then investigated two shRNAs targeting different regions of KDM2B. We found that sh-KDM2B#1 only targets KDM2B-1, whereas sh-KDM2B#2 effectively targets KDM2B-2. Our results showed that OGT protein levels were significantly increased in cells stably expressing sh-KDM2B#1 and #2 without affecting their mRNA expression, suggesting that KDM2B negatively regulates OGT protein levels and that the JmjC domain-encoded histone demethylase activity of KDM2B is not required for this function (Fig. 6D, E). Furthermore, our Co-IP results confirmed the interaction between OGT and KDM2B (Fig. 6F). Next, we examined whether KDM2B controls OGT protein stability. Treatment of the cells with 26S proteasome inhibitor MG132 effectively blocked OGT degradation, confirming that OGT was degraded through the proteasome pathway (Fig. 6G). Importantly, the knockdown of KDM2B effectively stabilized OGT expression and prolonged its half-life (Fig. 6H).

Fig. 6 | KDM2B may be involved in the regulation of OGT ubiquitination. A Plot of the results of the OGT ubiquitinated E3 ligase predicted by UbiBrowser 2.0. B qRT-PCR and WB were used to detect the mRNA and protein expression levels of KDM2B in MCAO mice, n = 6. Results are expressed as group mean ± standard deviation. *p < 0.05 vs. Sham group. C qRT-PCR and WB were used to detect the mRNA and protein expression levels of KDM2B in OGD/R-induced HT-22 cells, n = 3. Results are expressed as group mean ± standard deviation. *p < 0.05 vs. OGD/R group. Sh-KDM2B was transfected into HT-22 cells. D Protein levels of KDM2B and OGT were determined by WB. E qRT-PCR and WB were used to detect the mRNA and protein levels of OGT in HT-22 cells after KDM2B knockdown, n = 3. Results are expressed as group mean ± standard deviation. *p < 0.05 vs. sh-NC group. F The method of Co-IP determined the link between endogenous OGT and KDM2B in HT-22 cells. G The cells were pretreated with MG123 and then treated with CHX (20 mg/L) for the indicated time, and the protein level of OGT was determined by WB. H HT-22 cells transfected with sh-KDM2B were treated with CHX (20 mg/L) for the indicated time, and the protein level of OGT was determined by WB.

The SCF$^{KDM2B/FBXL10}$ complex functions as an OGT ubiquitinated E3 ligase to regulate OGT

In order to determine the mechanism by which KDM2B negatively regulates OGT, it has been confirmed that KDM2B can participate in the regulation of substrate protein ubiquitination in the form of a complex. The potential binding proteins of KDM2B were predicted by the PPI database, and the possibility that KDM2B promoted OGT degradation through its F-box binding to SKP1 and CUL1 was examined (Fig. 7A). We first determined whether CUL1 affects OGT protein levels. We found that the knockdown of CUL1 with two different siRNAs resulted in increased OGT protein levels (Fig. 7B). Similarly, inhibition of KDM2B or CUL1 also resulted in increased OGT protein expression. Furthermore, the co-deletion of KDM2B and CUL1 did not result in an additional increase in OGT protein levels, suggesting that KDM2B and CUL1 function in the same pathway that controls OGT (Fig. 7C). Taken together, these results suggest that KDM2B plays a major role in targeting OGT protein degradation via CUL1-based E3 ligases. Following the generally accepted nomenclature, we refer to the KDM2B-CUL1 E3 ligase as SCF$^{KDM2B/FBXL10}$.

To demonstrate that KDM2B assembles the SCF^{KDM2B} ligase complex to target OGT ubiquitination, we examined its interaction with components of the endogenous SCF E3 ligase complex. Co-IP assay showed that FLAG-tagged KDM2B interacted with endogenous SKP1, CUL1, and ROC1 (Fig. 7D). Previous structural analyses have shown that the N-terminal region of the F-box domain of SKP2 is essential for its binding to SKP1[25]. Similar to SKP2, the deletion of 23 amino acids from KDM2B (residues 1056 to 1078, called ΔF23) in the N-terminal half of the F-box domain significantly reduced CUL1 binding. Deletion of 48 residues (residues 1057–1105, ΔF48) containing the entire F-box domain completely abolished its binding to CUL1 (Fig. 7E). Taken together, these results suggest that KDM2B assembles a bona fides SCF-type E3 ubiquitin ligase complex through its F-box domain. Deletion of the F-box from KDM2B (ΔF48) also reduced the interaction between KDM2B and c-Fos (Fig. 7F). These findings suggest that the primary interaction between KDM2B and the substrate OGT is mediated by its LRRs domain, while the F-box domain may also play a role in this binding. To demonstrate the ubiquitylation of OGT by the SCF^{KDM2B} E3 ligase, we carried out both in vivo and in vitro ubiquitylation assays. We first knocked down either CUL1 or KDM2B and found that knocking down either gene reduced the ubiquitylation of endogenous OGT (Fig. 7G).

In vitro and in vivo assays verified that KDM2B regulates ferroptosis through OGT O-GlcNAcylation pathway to affect neuronal injury

To investigate the potential neuroprotective and anti-inflammatory effects of KDM2B through OGT-mediated regulation of ferroptosis, we established three models: OGD/R, OGD/R + sh-KDM2B, and OGD/R + sh-KDM2B + OSMI-1. Firstly, we assessed the viability of HT-22 cells in these groups using CCK-8 assay and EDU staining. Treatment with sh-KDM2B effectively restored cell damage induced by OGD/R, while this therapeutic effect was reversed upon co-treatment with OSMI-1 (Fig. 8A, B). CytoTox-Glo cytotoxicity assays showed that OSMI-1 reversed the therapeutic effect of sh-KDM2B on OGD/R-induced cell death (Fig. 8C). Consistently, similar trends were observed at the protein expression level of NeuN and PSD95 (Fig. 8D). Immunofluorescence analysis revealed that sh-KDM2B significantly reduced ROS levels and increased GSH content, which were both reversed by co-treatment with OSMI-1 (Fig. 8E, F). Furthermore, when BV2 cells were treated with culture media from the three groups, we found that TNF-α levels decreased while IL-10 levels increased in the OGD/R + sh-KDM2B group compared to the OGD/R group. However, these changes were reversed upon treatment with OSMI-1 (Fig. 8G).

Similarly, our study aimed to validate the role of the KDM2B-OGT axis in an in vivo model of MCAO (Supplementary Fig. 4). Treatment with sh-KDM2B effectively ameliorated MCAO-induced ischemic area and nerve damage, as evidenced by our ischemic and nerve damage scores. Notably, these beneficial effects were reversed upon OSMI-1 treatment (Fig. 9A, B).

The results were further confirmed through brain edema assessment and tissue staining (Fig. 9C, D). To gain deeper insights into neuronal damage, we separately examined the expression of NeuN and PSD95 (Fig. 9E). Interestingly, OSMI-1 treatment counteracted the significant therapeutic effect after KDM2B knockdown, which was consistent with our behavioral examination findings in mice (Fig. 9F). In order to verify the involvement of SLC7A11-induced ferroptosis, we measured levels of GSH and ROS. Remarkably, sh-KDM2B increased GSH levels while inhibiting ROS production; however, this effect was reversed upon the addition of OSMI-1 (Fig. 9G). Furthermore, TNF-α expression significantly decreased while IL-10 expression significantly increased in the sh-KDM2B group; however, this trend was reversed following the addition of OSMI-1 (Fig. 9H). Collectively, these results provide further confirmation that KDM2B-regulated OGT ubiquitination can impact neuronal injury and inflammatory response after stroke via the ferroptosis pathway both in vitro and in vivo.

Discussion

This study provides comprehensive evidence demonstrating the efficacy of OGT in improving ischemic area and neuronal damage in both in vitro and in vivo models, including MCAO and OGD/R. Additionally, we conducted the investigation into the role of OGT-mediated O-GlcNAcylation of SCL7A11 in regulating ferroptosis for stroke treatment. Furthermore, our findings indicate that overexpression of OGT also mitigates stroke-induced microglial inflammation. Importantly, this study unveils a novel mechanism involving the KDM2B complex promoting ubiquitination of OGT, elucidating the underlying cause for altered expression levels observed in the MCAO model (Fig. 9I). Moreover, we identified the specific domain within KDM2B responsible for regulating OGT ubiquitination and confirmed that KDM2B is regulated through the ubiquitination pathway rather than histone methylation pathway.

Cysteine serves as the rate-limiting precursor for glutathione biosynthesis. Recent investigations have substantiated that most cells can acquire cysteine from the extracellular milieu via nutrient transporters[11,12,26]. In this study, we assessed the level of cystine uptake in HT-22 cells treated with OGT and observed that OGT reinstated the diminished cystine levels induced by OGD/R. These findings suggest a crucial role of OGT in facilitating the cellular uptake of cystine from the extracellular environment, thereby maintaining its activity. System xc- functions as a cystine/glutamate antiporter responsible for mediating intracellular entry of cystine in exchange for glutamate molecules[27]. Certain ferroptosis-inducing drugs like sorafenib and erastin inhibit SLC7A11-mediated transport of cysteine into cells to promote ferroptosis[28]. Studies have demonstrated that inhibition of ferroptosis can ameliorate neuronal death caused by stroke[29–31]. Although previous studies have reported decreased expression of OGT in MCAO models, neither the therapeutic effects nor mechanisms underlying OGT in MCAO have been confirmed thus far[32,33]. In this study, we elucidate the mechanisms by which overexpression of OGT ameliorates motor function deficits and neuronal damage.

The cysteine-glutamate transport system xc- is composed of a heterodimer comprising the light chain subunit SLC7A11 and the heavy chain subunit SLC3A2. Extracellular cystine enters the cell through SLC7A11, while SLC3A2 serves as an anchor for SLC7A11 on the plasma membrane and maintains its stability (Fig. 4B). Additionally, we observed that O-GlcNAcylation of SLC7A11 by OGT in HT-22 cells is crucial for its cystine uptake function. This study further confirms that O-GlcNAcylation occurs at residue S26 of SLC7A11 mediated by OGT. Furthermore, it should be noted that O-GlcNAc is a prevalent, dynamic, and inducible post-translational modification occurring on serine and threonine residues, regulating various protein functions. Emerging evidence suggests alterations in O-GlcNAcylation associated with diseases. We demonstrate reduced overall levels of O-GlcNAc acylation as a common feature in HT-22 cells subjected to OGD/R, which aligns with our previous findings. O-GlcNAcylation has been reported to play diverse roles in ferroptosis; for instance, c-Jun's O-GlcNAc acylation stimulates glutathione synthesis and
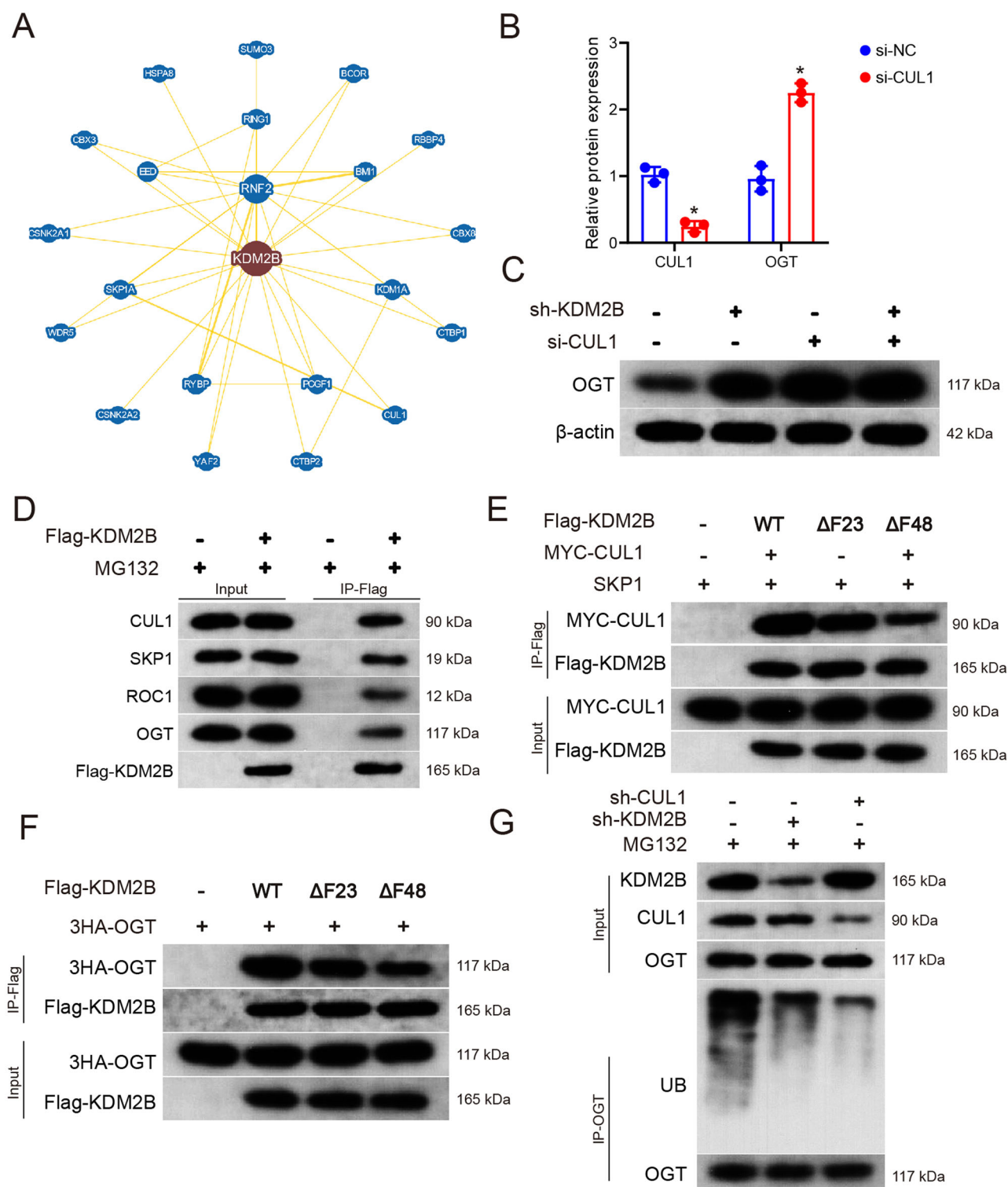
Fig. 7 | The SCF$^{KDM2B/FBXL10}$ complex functions as an OGT ubiquitinated E3 ligase to regulate OGT. A PPI network diagram of KDM2B interacting proteins predicted by BioGRID. **B** HT-22 cells were transfected with si-CUL1, and the expression of CUL1 and OGT proteins was determined by WB. $n = 3$. Results are expressed as group mean ± standard deviation. *$p < 0.05$ vs. sh-NC group. **C** HT-22 cells were transfected with sh-KDM2B and si-CUL1 alone or in combination, and the expression of OGT protein was determined by WB. **D** HT-22 cells were transfected with a plasmid expressing FLAG-tagged KDM2B and treated with 20 μM MG132 for 6 h. The interaction of KDM2B with the endogenous proteins CUL1, SKP1, ROC1, and OGT was determined by Co-IP. **E** HT-22 cells were transfected with plasmids expressing the indicated proteins, and the interaction of KDM2B-WT or different mutants with CUL1 was determined by Co-IP. **F** HT-22 cells were transfected with plasmids expressing the indicated proteins, and the interaction of KDM2B-WT or different mutants with OGT was determined by Co-IP. **G** HEK293 cells were transfected with sh-KDM2B and si-CUL1 and treated with 20 μM MG132 for 6 h. Endogenous OGT was immunoprecipitated and immunoblotted with an anti-ubiquitin-specific antibody.
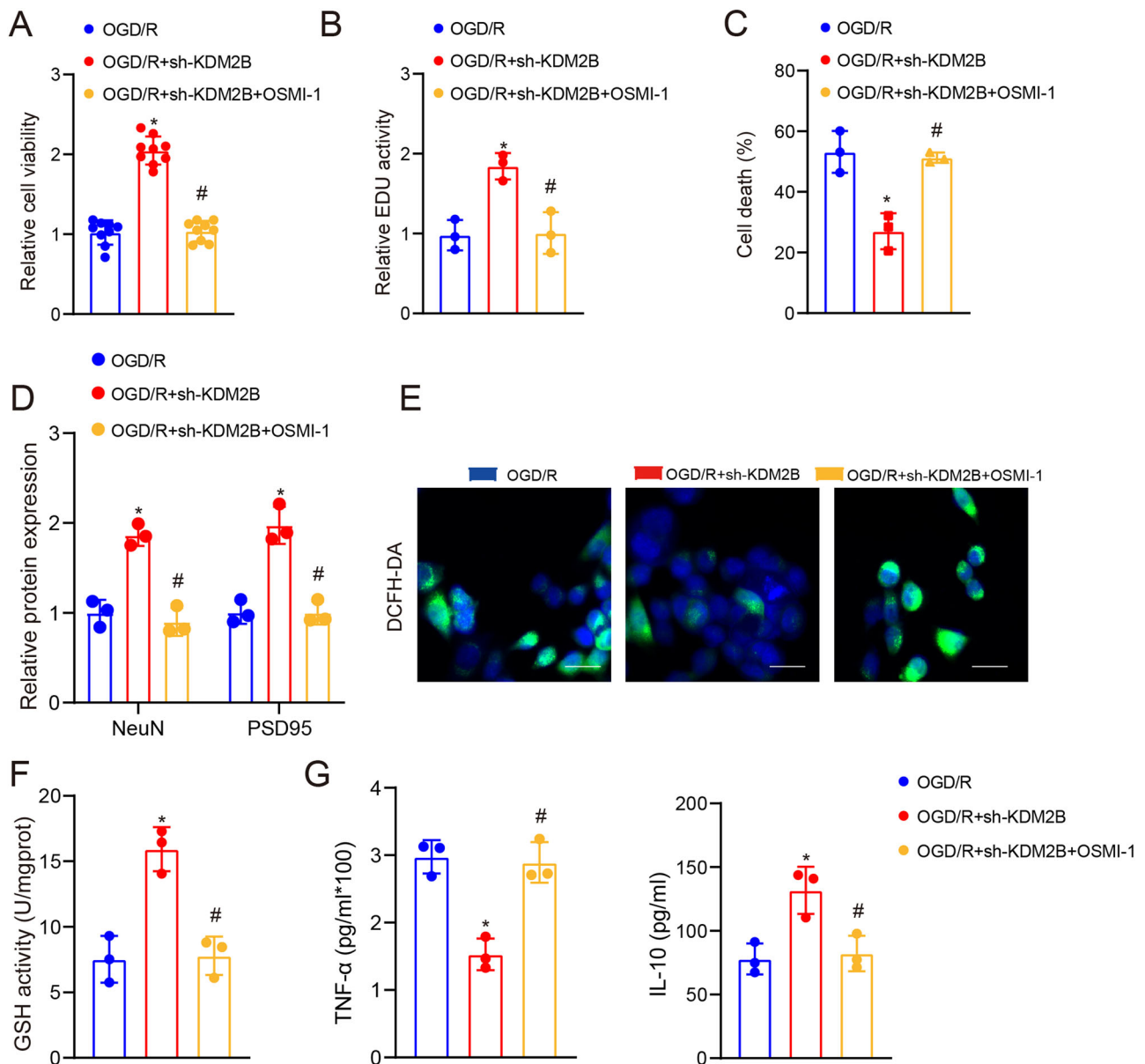
Fig. 8 | In vitro models verified that KDM2B regulates ferroptosis through OGT O-GlcNAcylation pathway to affect neuronal injury. OGD/R-induced HT-22 cells were transfected with Sh-KDM2B or treated with OSMI-1 and divided into OGD/R group, OGD/R + Sh-KDM2B group, and OGD/R + Sh-KDM2B + OSMI-1 group. **A** CCK-8 was used to detect cell viability in different groups. $N = 3$. **B** EDU staining was used to detect the proliferation ability of cells in different groups, $N = 3$. **C** CytoTox-Glo cytotoxicity assays were used to detect the cell death rate of each treatment group. **D** The protein expression levels of NeuN and PSD95 in different groups were detected by WB, $n = 3$. **E** Fluorescence staining of ROS in different groups with DCHH-DA. Scale bar: 20 μM. **F** GSH content was measured in different groups, $n = 3$. **G** The contents of THF-α and IL-10 in different groups were determined, $n = 3$. Results were expressed as group mean ± standard deviation. *$p < 0.05$ vs. OGD/R group; #$p < 0.05$ vs. OGD/R + sh-KDM2B group.

reduces ROS accumulation to inhibit ferroptosis[34]. Moreover, inhibiting YAP degradation via antagonizing Ser127 phosphorylation through O-GlcNacylation leads to increased Fe2+ concentration and lipid peroxidation[35]. In this study, we identify an additional pathway regulating ferroptosis following MCAO.

To investigate the underlying mechanism of OGT changes, we observed that its mRNA remained unchanged, indicating a potential role for post-translational modification. Ubiquitination, achieved through the ubiquitin-proteasome system (UPS), is a prominent cellular pathway for protein degradation. Following stroke, an extensive loss of neurons and glial cells occurs, necessitating the crucial role of UPS in eliminating damaged proteins and maintaining cellular homeostasis. However, excessive UPS activity can also result in aberrant degradation of normal proteins, exacerbating neuronal damage. Studies have demonstrated the close association

between ubiquitination and post-stroke inflammatory response. Certain ubiquitinated proteins are capable of modulating the expression and release of inflammatory factors, thereby influencing stroke progression. For instance, investigation into USP25 (deubiquitinating protease 25) revealed that inhibition of its activity could enhance motor recovery and cognitive function improvement in mouse models of stroke by suppressing glia-mediated inflammation[36]. Our bioinformatics analysis led us to identify KDM2B as a plausible ubiquitinated E3 ligase involved in this process. Interestingly, KDM2B possesses a JmjC domain responsible for histone H3K36 demethylation, thus revealing an additional enzymatic activity of this multidomain protein[37,38]. Our findings highlight its ability to modulate OGT expression through regulation of its ubiquitination status. Previous studies have already established the role of KDM2B as an E3 ligase involved in cognitive impairment regulation[38,39]; Our data also suggest that KDM2B is
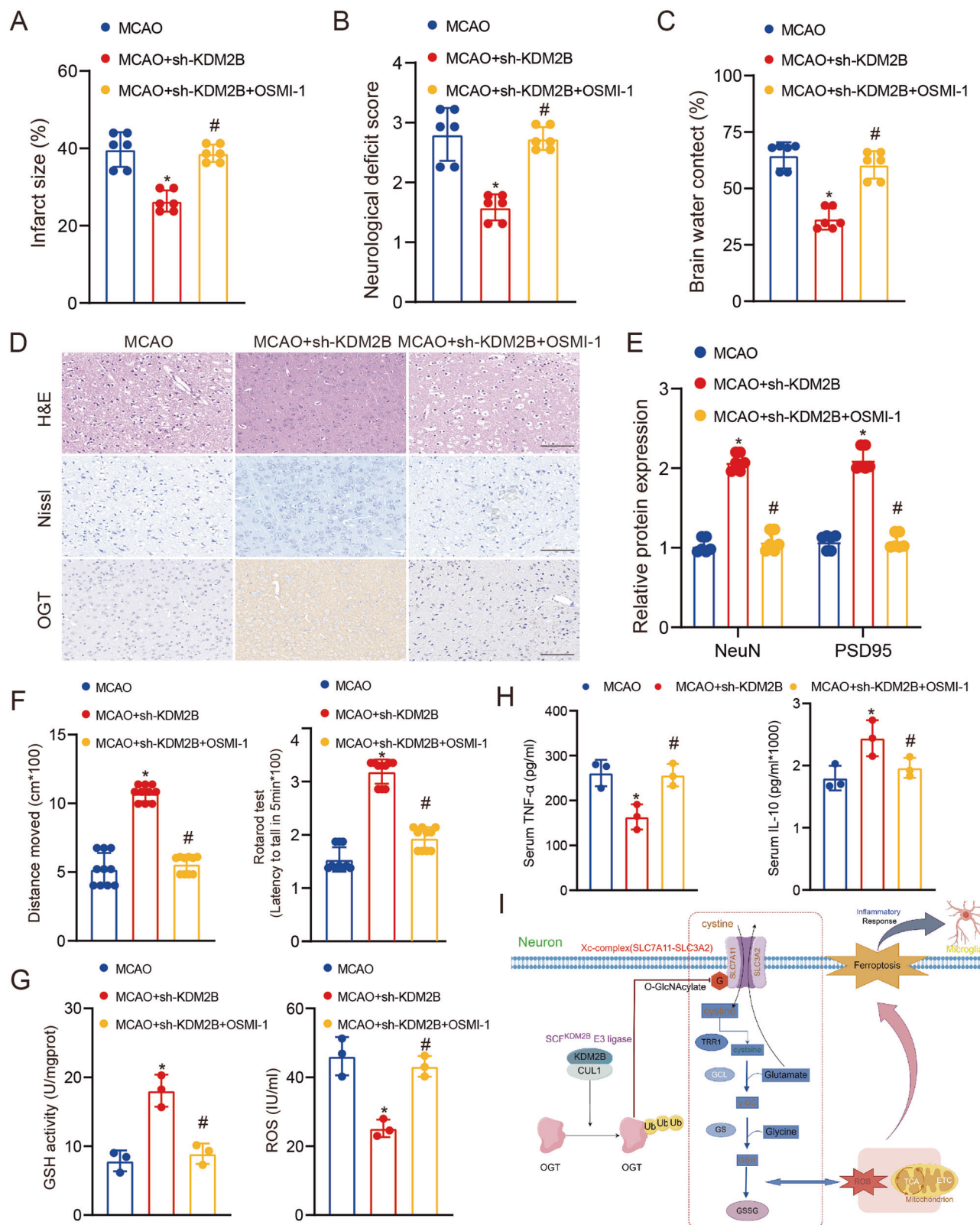
Fig. 9 | In vivo models verified that KDM2B regulates ferroptosis through OGT O-GlcNAcylation pathway to affect neuronal injury. KDM2B knockdown MCAO mice were constructed and treated with OSMI-1. The mice were divided into the MCAO group, MCAO + sh-KDM2B group, and MCAO + sh-KDM2B + OSMI-1 group. **A** Statistical analysis of cerebral infarct size in different groups, $n = 6$. **B** Nerve injury scores in different groups, $n = 6$. **C** Statistics of hydrocephalus in different groups, $n = 6$. **D** The brain tissues of different groups were stained with HE and Nissl staining, and the protein expression of OGT in different groups was detected by immunohistochemistry. Scale bar: 100 μm. **E** The protein expression levels of NeuN and PSD95 in different groups were detected by WB, $n = 6$. **F** Open field-testing and rotarod test in different groups of mice, $n = 10$. **H** The contents of THF-α and IL-10 in different groups were determined, $n = 3$. **G** GSH and ROS contents were measured in different groups, $n = 3$. **I** The mechanism roadmap. Results were expressed as group mean ± standard deviation. *$p < 0.05$ vs. MCAO group; #$p < 0.05$ vs. MCAO + Sh-KDM2B group.

implicated in the regulation of OGT ubiquitination in brain injury. Numerous studies have demonstrated the involvement of KDM2B in mechanisms related to nervous system diseases and tumors[40–43]; however, further extensive data are required to explore potential side effects following KDM2B silencing. Additionally, we aim to employ network pharmacology for screening potential therapeutic drugs targeting KDM2B in order to expedite its clinical application feasibility. O-GlcNAcylation and ubiquitination, as crucial post-translational modifications of proteins, play distinct roles in stroke[44,45]. While O-GlcNAcylation may mitigate cerebral ischemic injury through its protective effect, ubiquitination might participate in the pathophysiological process of stroke via protein degradation and signal transduction pathways[44,45]. Investigating the interaction and co-regulation between these two modifications holds significant importance for stroke treatment and rehabilitation efforts. Future research should focus on elucidating specific mechanisms and potential targets associated with these two modifications in stroke, thereby providing novel ideas and approaches for stroke prevention and treatment.

In conclusion, our study demonstrates the therapeutic efficacy of OGT in ameliorating motor deficits and neuronal damage post-stroke through the regulation of SLC7A11 O-GlcNacylation-mediated ferroptosis. Furthermore, we validate that alterations in OGT levels are mediated by the KDM2B-mediated ubiquitination pathway. These findings provide a crucial foundation for target selection and biomarker identification in stroke treatment.

Material and methods
Reagents and antibodies
Antibodies against FLAG (SG4110-16, Shanghai Genomics Technology), β-actin (A00702, 1:1000, GenScript), HA (sc-7392, Santa Cruz), KDM2B (09-864, 1:500, Millipore), CUL1 (ab75817, 1:1000, Abcam), SKP1 (ab80586, 1:1000, Abcam), ROC1 (ab221548, 1:1000, Abcam), Ubiquitin (Z045801-5, Dako), SLC7A11 (26864-1-AP, 1:1000, Proteintech), OGT (ab96718, 1:1000, Abcam), O-GlcNAcylation (sc-59623, 1:1000, Santa Cruz), NeuN (ab104224, 1:1000, Abcam), PSD95 (ab18258, 1:1000, Abcam), CD206 (ab64693, 1:1000, Abcam), CD86 (#91882, 1:1000, Cell Signaling Technology), Iba1 (019-19741, 1:500, Wako), MG132 (C2211, Sigma–Aldrich), CHX (94271, AMRESCO), Thiamet-G (S7213, Selleck), OSMI/1 (S9835, Selleck).

Animals and transient middle cerebral artery occlusion (MCAO)
All C57BL/6 mice aged 8–10 weeks were purchased from Beijing Charles River Laboratory Animal Company and housed in a pathogen-free facility under a 12-h light/dark cycle with AD libitum access to food and water. All animal studies were performed in accordance with the Ethical Guidelines for the Use and Care of Laboratory Animals and were approved by the Animal Ethics Committee of Sichuan Provincial People's Hospital. We have complied with all relevant ethical regulations for animal use.

All mice were fasted for 6 h but could not refrain from drinking. The purpose of fasting the mice for 6 h was to eliminate any potential impact on stroke progression caused by variations in blood glucose levels and simulate human preoperative fasting while ensuring that starvation did not affect the results[29,46,47]. MCAO model was established by the internal carotid artery occlusion method. The mice were anesthetized by intraperitoneal injection of 60 mg/kg pentobarbital and fixed in the prone position. The neck was disinfected and a 1.5 cm incision was cut in the middle of the neck. The subcutaneous tissue, glands, and muscles were separated, and the right common carotid artery and internal carotid artery were exposed.

A knot was tied at both ends of the external carotid artery, a small incision was cut between the two knots, a thread plug was inserted, and the external carotid artery was pulled, so that the thread plug slowly entered the internal carotid artery about 10 mm or so if slight resistance was encountered, the entry was stopped. The thread plug was fixed, the incision was sutured layer by layer, and the thread plug was disinfected to prevent infection. Laser Doppler flowmetry was utilized for monitoring regional cerebral blood flow. The confirmation of interrupted blood flow in the

middle cerebral artery occurred when cerebral blood flow decreased to less than 25% of its initial level. Following 60 min period of obstruction, the filament was removed and restoration of cerebral blood flow to over 70% of its baseline value confirmed reperfusion. Subsequent assays were performed 24 h after reperfusion. In the sham operation group, the operation was the same as MCAO, but the suture plug only penetrated about 5 mm, without causing cerebral ischemia. This study was divided into two parts according to the purpose of the study. The first part was to verify the regulatory effect of OGT overexpression on MCAO. The study was divided into three groups (Sham group, MCAO + NC group, MCAO + OGT group) with 18 mice in each group. The second part was to verify the regulatory effect of KDM2B on MCAO, with 18 mice in three groups (MCAO group, MCAO + sh-KDM2B group, MCAO+sh-KDM2B + OSMI-1). The testing procedure for all animals is shown in Fig. 1A.

In this study, Longa's method was employed to assess the neurological deficits of experimental rats in each group 24 h post-modeling. The specific scoring criteria were as previously described[48–50]: (1) absence of neurological deficit: 0; (2) incomplete extension of the paralyzed forepaw: 1 point; (3) turning towards the paralyzed side while walking: 2 points; (4) falling towards the paralyzed side during ambulation: 3 points; (5) inability to walk autonomously with loss of consciousness: 4 points. Animals with scores greater than or equal to 3 were selected for subsequent testing.

Evaluation of motor function in mice
Open field-testing. The locomotor activity was evaluated on days 7 after MCAO, following the same methodology as previously reported[51]. The mice were placed in a well-lit enclosure measuring 50 cm wide × 50 cm length × 38 height and allowed to freely explore for a duration of 5 min. Overhead recording was conducted throughout the experiment, and subsequently, Noldus Ethovision behavior software was employed for video analysis.

Rotarod test. Before the experiment, mice were first placed on a horizontally rotating rod and given a certain amount of adaptation time. Subsequently, the experiment began with the rotards rotating at a constant speed, and the mice needed to maintain their balance and move along with the rotards movement. During the experiment, the performance of the mice on the rotarod was observed and recorded, including whether they could maintain balance and the duration of continuous stay on the rotarod.

2, 3, 5-triphenyltetrazolium Chloride (TTC) Staining
Infarct volume was determined using 2,3,5-triphenyltetrazolium chloride (TTC) staining. Coronal brain sections (1 mm thick) were immersed in a 2% TTC solution for 20 min at 37 °C. The infarcted and non-infarcted hemispheres were analyzed using ImageJ software (National Institutes of Health, USA).

Construction of an oxygen-glucose deprivation/reoxygenation (OGD/R) model
Mouse neuronal cells HT-22 were purchased from Wuhan Procell Biotechnology Co., LTD. HT-22 cells were cultured in DMEM medium (PM150270, Procell, China) for 3 h at 37 °C under hypoxic conditions (1% O_2, 94% N_2, 5% CO_2), and then changed to normal oxygen supply (95% air, 5% CO_2) medium containing sugar for 24 h. Normal cultured HT-22 cells were used as control.

Cell viability assay
The Cell Counting Kit-8 (CCK-8) (Bimake Catalog number B34302) was utilized to perform cell viability experiments, following the manufacturer's instructions. Cells were seeded at a density of 1×10^4 cells/well in 96-well plates and treated with varying concentrations of compounds for specified durations. Subsequently, each well received 10 μl of CCK-8 reagent and was incubated for 2 h in a humidity-controlled incubator maintained at 37 °C

and 5% CO_2. The absorbance at 450 nm was measured using a microplate reader. All experiments were conducted thrice.

CytoTox-Glo™ cytotoxicity assay
Cell viability was determined using CytoTox-Glo (G9290, Promega, Mannheim, Germany). This assay measures the dead-cell protease activity, which is released from cells that have lost membrane integrity. The assay uses a luminogenic peptide substrate (alanyl-alanyl-phenylalanyl-amino-luciferin, AAF-Glo Substrate) to measure dead-cell protease activity. Cells were seeded before treatment in black poly-d-lysine-coated 384-well plates. Compounds were added to the cells in a final DMSO concentration of 0.8% and cells were incubated for 22 h. Prewarmed CytoTox-Glo reagent was added to the medium (1:5 dilution) and cells were incubated for 15 min at room temperature. Prior to measurement, plates were gently shaken and cell cytotoxicity was measured in an EnVision Multilabel Reader (PerkinElmer, Waltham, MA). Data were analyzed using Microsoft Excel (Microsoft Corp., Redmond, WA). Graphs were assembled using GraphPad Prism 6.0 (GraphPad Software, Inc., La Jolla, CA).

Quantitative real time-PCR (QRT-PCR)
TRIzol was employed to extract total RNA. The PrimeScript TM RT Reagent Kit with gDNA Eraser (RR047B, Takara, Shandong, China) was utilized for cDNA synthesis in order to eliminate genomic DNA. Quantification of RNA levels was performed using the SYBR Green qPCR Mix (RR820B, Takara). Supplementary Table 1 was used to present the gene primer sequences.

Plasmid construction and lentiviral infection
The plasmids were generated through the cloning of the corresponding cDNA into the respective expression vector using designed primers. For shRNA, viruses were produced by harvesting the viral supernatant from transfected HEK293T cells 48–72 h post-transfection and subsequently used to infect target cells at a confluence of 70%. KDM2B and CUL1 knockout (KO) cell lines were established utilizing the lentiCRISPR method. In brief, the lentiviral CRISPR vector was linearized with BsmBI for guide RNA (shRNA) construction in the lentiviral expression vector of lentiCRISPR V2.sh-KDM2B #1: TGAGCGTGAAAGGTTGTTT; sh-KDM2B #2: GCCTTTACAAGAAGA CATT ; si-CUL1: GGCCACUGAAUAAACAGGUAACAAA.

Western blot (WB)
Cells were harvested and lysed with SDS loading buffer. In vivo, assays were conducted to isolate certain proteins from the peri-infarct region of mice. The resulting proteins were separated by SDS-PAGE electrophoresis and transferred onto a PVDF membrane, which was subsequently blocked with 5% non-fat milk. The PVDF membrane was then incubated with specific primary antibodies. After incubation with secondary antibodies, the proteins were observed by chemiluminescence. ImageJ software was used for protein gray value analysis.

EdU proliferation assay
The cellular proliferation was assessed using the EdU kit (provided by KeyGen Biotech Co., Ltd.) to quantify the EdU incorporation. After 48 h of transfection, cells were seeded at a density of 2×10^5 cells per well in a 6-well plate and exposed to 10 nM EdU for a duration of 12 h. Subsequently, the cells were fixed and permeabilized with 0.5% Triton X-100 for a period of 20 min. Following this, the Click-iT reaction cocktail was introduced, and the cells were incubated under dark conditions for approximately half an hour. After two washes with PBS, DAPI dye was applied as a counterstain for about ten minutes in darkness before observing them using fluorescence microscopy.

Determination of intracellular ROS and malondialdehyde (MDA)
The CellROX™ Deep Green Reagent (Invitrogen, C10444) is employed in the experimental procedure to observe fluorescence microscopy and detect intracellular levels of ROS. Briefly, prior to treatment, samples are exposed

to a 5 μM solution of the reagent for a duration of 30 min. Subsequently, after a post-treatment period lasting 0.5 h, cells are gathered for measurements of fluorescence intensity. The intracellular levels of malondialdehyde (MDA) were determined using MDA detection kits provided by Solarbio Science & Technology Co., Ltd., Beijing, China.

GSH and cysteine assay
The Glutathione Assay Kit (Beyotime, S0053) was utilized to evaluate the relative concentration of GSH, following the provided instructions from the manufacturer. In brief, a kinetic assay was employed to measure GSH levels by observing its catalytic effect on reducing 5,5′-dithiobis (2-nitrobenzoic acid) into 5-thio-2-nitrobenzoic acid. The generated GSSG was then recycled using GSR/glutathione reductase and NADPH. The reaction rate exhibited linearity with glutathione concentrations up to 2 mM. Spectrophotometric analysis at 412 nm allowed for quantification of the resulting yellow product (5-thio-2-nitrobenzoic acid). To assess the relative cysteine concentration, we followed the manufacturer's instructions provided in the Cysteine Assay Kit (Sigma, MAK255).

Intracellular iron assay
The concentration of ferrous ions within the cell was assessed by utilizing FerroOrange dye (#F374, Dojindo Laboratories). Cells were cultured and subjected to specific treatments. Subsequently, a diluted solution (1:2000, v/v) of FerroOrange Orange dye was added to the cells and incubated at 37 °C for 30 min. Fluorescent images were captured using a confocal microscope.

Immunoprecipitation (IP)
One-fifth of the cells that underwent transfection were directly utilized for Western blot analysis, while the remaining cells were lysed using Co-IP lysis buffer. After a 40-min lysis period, centrifugation was performed at 12,000 rpm and 4 °C for 20 min to separate cellular debris. The resulting supernatant was then subjected to overnight incubation with ANTI-FLAG M2 Affinity Gel beads (Sigma, M8823) at a temperature of 4 °C. Subsequently, three washes were conducted before boiling the beads and analyzing the eluted proteins through WB.

In vivo ubiquitination assay
In the ubiquitination experiments, cells were transfected with the specified plasmids for a duration of 36 h. Following this, they were treated with MG132 at a concentration of 20 μM for an additional period of 8 h. Subsequently, the cells were collected. A portion equivalent to one-fifth of the cells was set aside for direct immunoblotting analysis, while the remaining cells underwent denaturing co-immunoprecipitation processing. The cell lysis was performed using denaturing buffer, and then incubated overnight with either Myc beads (Millipore; E6654) or HA-beads (Millipore; IP0010) at a temperature of 4 °C. Following this step, thorough washing of the beads was carried out using buffers and Buffer C consecutively.

Hematoxylin and eosin (HE) staining
The prepared paraffin sections of brain tissue were incubated at 60 °C for 3 h, followed by hematoxylin staining for 2 min and subsequent washing. Eosin staining was performed on the sections at room temperature for 1 min. The samples underwent dehydration using a gradient alcohol series, were cleaned with xylene, sealed with neutral glue, and subsequently observed under a microscope and photographed.

Immunohistochemical (IHC) staining
The immunohistochemical staining was conducted following the instructions provided with the immunohistochemistry kit. To assess the stainings, quantitative imaging techniques were employed to record both the percentage and intensity of immunostaining.

Enzyme-linked immunosorbent assay (ELISA)
The levels of cytokines in the supernatants obtained from ischemic brain tissues were quantified using ELISA array Kit (Qiagen, Duesseldorf,

Germany) as previously described. These kits allow for the detection of 5 different cytokines including interleukin [IL]−1α, IL-1β, IL-4, IL-10, and tumor necrosis factor [TNF]-α. The manufacturer's instructions were followed to perform the assays under uniform conditions. Duplicate measurements were conducted on individual mouse brains and the results were expressed as average optical density (OD) values.

Immunofluorescence staining
The frozen coronal sections of rat brains in the ischemia penumbra were achieved 24 h after MCAO for NeuN staining. The following antibodies were used: mouse anti-NeuN (Abcam, ab252833, 1:100) and Alexa-488 (Abcam, ab150105, 1:200) donkey anti-mouse secondary antibody. The total numbers of NeuN-positive neurons in the ischemic penumbra were counted in five different fields of view for each section by a researcher who was blinded to the groupings.

Statistical analysis
Data were obtained from at least three independent experiments. All statistical analyses were conducted using GraphPad Prism 9.0.0 software. Unless otherwise stated, all data are presented as mean ± standard deviation. Statistical significance of differences was determined using two-tailed Student's t-tests. One-way analysis of variance (ANOVA) was used for three or more groups, and the Tukey method was used for post-hoc pairwise comparison. All p-values are two-sided, and a p-value < 0.05 was considered statistically significant.

Reporting summary
Further information on research design is available in the Nature Portfolio Reporting Summary linked to this article.

Data availability
The datasets have been uploaded in accordance with the journal's requirements (Supplementary Data 1), and any data utilized and/or analyzed during this study are available from the corresponding authors upon reasonable request.

References
1. Toman, N. G., Grande, A. W. & Low, W. C. Neural repair in stroke. *Cell Transpl.* **28**, 1123–1126 (2019).
2. Guzik, A. & Bushnell, C. Stroke epidemiology and risk factor management. *Continuum* **23**, 15–39 (2017).
3. Diener, H. C. et al. Review and update of the concept of embolic stroke of undetermined source. *Nat. Rev. Neurol.* **18**, 455–465 (2022).
4. Esenwa, C. & Gutierrez, J. Secondary stroke prevention: challenges and solutions. *Vasc. Health Risk Manag.* **11**, 437–450 (2015).
5. Guo, J., Tuo, Q. Z. & Lei, P. Iron, ferroptosis, and ischemic stroke. *J. Neurochem* **165**, 487–520 (2023).
6. Fu, C. et al. Rehmannioside A improves cognitive impairment and alleviates ferroptosis via activating PI3K/AKT/Nrf2 and SLC7A11/GPX4 signaling pathway after ischemia. *J. Ethnopharmacol.* **289**, 115021 (2022).
7. Hu, X., Bao, Y., Li, M., Zhang, W. & Chen, C. The role of ferroptosis and its mechanism in ischemic stroke. *Exp. Neurol.* **372**, 114630 (2024).
8. Liu, C., Li, Z. & Xi, H. Bioinformatics analysis and in vivo validation of ferroptosis-related genes in ischemic stroke. *Front Pharmacol.* **13**, 940260 (2022).
9. Tuo, Q. Z. et al. Thrombin induces ACSL4-dependent ferroptosis during cerebral ischemia/reperfusion. *Signal Transduct. Target Ther.* **7**, 59 (2022).
10. Zheng, D. et al. ROS-triggered endothelial cell death mechanisms: focus on pyroptosis, parthanatos, and ferroptosis. *Front Immunol.* **13**, 1039241 (2022).
11. Chen, X., Li, J., Kang, R., Klionsky, D. J. & Tang, D. Ferroptosis: machinery and regulation. *Autophagy* **17**, 2054–2081 (2021).
12. Koppula, P., Zhuang, L. & Gan, B. Cystine transporter SLC7A11/xCT in cancer: ferroptosis, nutrient dependency, and cancer therapy. *Protein Cell* **12**, 599–620 (2021).
13. Shen, L. et al. PHGDH inhibits ferroptosis and promotes malignant progression by upregulating SLC7A11 in bladder cancer. *Int. J. Biol. Sci.* **18**, 5459–5474 (2022).
14. Yang, Y. et al. STAT6 inhibits ferroptosis and alleviates acute lung injury via regulating P53/SLC7A11 pathway. *Cell Death Dis.* **13**, 530 (2022).
15. Zhang, L. et al. RAGE signaling pathway is involved in CUS-induced depression-like behaviors by regulating the expression of NR2A and NR2B in rat hippocampus DG. *Exp. Neurol.* **361**, 114299 (2023).
16. Yang, Z. et al. OGT/HIF-2α axis promotes the progression of clear cell renal cell carcinoma and regulates its sensitivity to ferroptosis. *iScience* **26**, 108148 (2023).
17. Tang, J. et al. Targeting USP8 inhibits O-GlcNAcylation of SLC7A11 to promote ferroptosis of hepatocellular carcinoma via stabilization of OGT. *Adv. Sci.* **10**, e2302953 (2023).
18. Tang, J. et al. The deubiquitinase EIF3H promotes hepatocellular carcinoma progression by stabilizing OGT and inhibiting ferroptosis. *Cell Commun. Signal.* **21**, 198 (2023).
19. Zhang, H., Zhang, J., Dong, H., Kong, Y. & Guan, Y. Emerging field: O-GlcNAcylation in ferroptosis. *Front. Mol. Biosci.* **10**, 1203269 (2023).
20. Xu, J. et al. Lactate attenuates astrocytic inflammation by inhibiting ubiquitination and degradation of NDRG2 under oxygen-glucose deprivation conditions. *J. Neuroinflammation* **19**, 314 (2022).
21. Zheng, S. et al. OTUD1 ameliorates cerebral ischemic injury through inhibiting inflammation by disrupting K63-linked deubiquitination of RIP2. *J. Neuroinflammation* **20**, 281 (2023).
22. Andricovich, J., Kai, Y., Peng, W., Foudi, A. & Tzatsos, A. Histone demethylase KDM2B regulates lineage commitment in normal and malignant hematopoiesis. *J. Clin. Invest.* **126**, 905–920 (2016).
23. Kang, J. Y. et al. KDM2B is a histone H3K79 demethylase and induces transcriptional repression via sirtuin-1-mediated chromatin silencing. *FASEB J.* **32**, 5737–5750 (2018).
24. Zacharopoulou, N. et al. The histone demethylase KDM2B activates FAK and PI3K that control tumor cell motility. *Cancer Biol. Ther.* **21**, 533–540 (2020).
25. Zheng, N. et al. Structure of the Cul1-Rbx1-Skp1-F boxSkp2 SCF ubiquitin ligase complex. *Nature* **416**, 703–709 (2002).
26. Lei, G., Mao, C., Yan, Y., Zhuang, L. & Gan, B. Ferroptosis, radiotherapy, and combination therapeutic strategies. *Protein Cell* **12**, 836–857 (2021).
27. Rochette, L. et al. Lipid peroxidation and iron metabolism: two corner stones in the homeostasis control of ferroptosis. *Int. J. Mol. Sci.* https://doi.org/10.3390/ijms24010449 (2022).
28. Liu, J., Kang, R. & Tang, D. Signaling pathways and defense mechanisms of ferroptosis. *FEBS J.* **289**, 7038–7050 (2022).
29. Cui, Y. et al. ACSL4 exacerbates ischemic stroke by promoting ferroptosis-induced brain injury and neuroinflammation. *Brain Behav. Immun.* **93**, 312–321 (2021).
30. Stockwell, B. R. et al. Ferroptosis: a regulated cell death nexus linking metabolism, redox biology, and disease. *Cell* **171**, 273–285 (2017).
31. Zhang, Y., Lu, X., Tai, B., Li, W. & Li, T. Ferroptosis and its multifaceted roles in cerebral stroke. *Front. Cell Neurosci.* **15**, 615372 (2021).
32. Luo, Y., Chen, P., Yang, L. & Duan, X. Metabolomic analysis and pharmacological validation of the cerebral protective effect of 3,4-dihydroxybenzaldehyde on cerebral ischemia-reperfusion injury. *Mol. Med. Rep.* https://doi.org/10.3892/mmr.2022.12896 (2023).

33. Zhao, J. et al. O-GlcNAc transferase (OGT) protects cerebral neurons from death during ischemia/reperfusion (I/R) injury by modulating Drp1 in mice. *Neuromolecular Med.* **24**, 299–310 (2022).

34. Chen, Y. et al. O-GlcNAcylated c-Jun antagonizes ferroptosis via inhibiting GSH synthesis in liver cancer. *Cell Signal.* **63**, 109384 (2019).

35. Zhai, L. et al. O-GlcNAcylation mediates endometrial cancer progression by regulating the Hippo-YAP pathway. *Int. J. Oncol.* https://doi.org/10.3892/ijo.2023.5538 (2023).

36. Li, Z. et al. USP25 inhibits neuroinflammatory responses after cerebral ischemic stroke by deubiquitinating TAB2. *Adv. Sci.* **10**, e2301641 (2023).

37. Fukuda, T., Tokunaga, A., Sakamoto, R. & Yoshida, N. Fbxl10/Kdm2b deficiency accelerates neural progenitor cell death and leads to exencephaly. *Mol. Cell Neurosci.* **46**, 614–624 (2011).

38. Han, X. R. et al. KDM2B/FBXL10 targets c-Fos for ubiquitylation and degradation in response to mitogenic stimulation. *Oncogene* **35**, 4179–4190 (2016).

39. Yang, Y. et al. FBXL10 promotes ERRα protein stability and proliferation of breast cancer cells by enhancing the mono-ubiquitylation of ERRα. *Cancer Lett.* **502**, 108–119 (2021).

40. Peta, E., Masi, G. & Barzon, L. KDM2B in papillomavirus-related cancer. *Oncoscience* **5**, 159–160 (2018).

41. van Jaarsveld, R. H. et al. Delineation of a KDM2B-related neurodevelopmental disorder and its associated DNA methylation signature. *Genet. Med.* **25**, 49–62 (2023).

42. Yan, M., Yang, X., Wang, H. & Shao, Q. The critical role of histone lysine demethylase KDM2B in cancer. *Am. J. Transl. Res.* **10**, 2222–2233 (2018).

43. Zhang, B. et al. KDM2B regulates hippocampal morphogenesis by transcriptionally silencing Wnt signaling in neural progenitors. *Nat. Commun.* **14**, 6489 (2023).

44. Gu, J. H. et al. O-GlcNAcylation reduces ischemia-reperfusion-induced brain injury. *Sci. Rep.* **7**, 10686 (2017).

45. Li, X. & Yang, W. Targeting O-GlcNAcylation in ischemic stroke. *Neural Regen. Res.* **17**, 2427–2428 (2022).

46. Liu, L. et al. Melatonin protects against focal cerebral ischemia-reperfusion injury in diabetic mice by ameliorating mitochondrial impairments: involvement of the Akt-SIRT3-SOD2 signaling pathway. *Aging* **13**, 16105–16123 (2021).

47. Ma, R. et al. Animal models of cerebral ischemia: a review. *Biomed. Pharmacother.* **131**, 110686 (2020).

48. Li, Y., Chu, L., Liu, C., Zha, Z. & Shu, Y. Protective effect of GSK-3β/Nrf2 mediated by dimethyl fumarate in middle cerebral artery embolization reperfusion rat model. *Curr. Neurovasc. Res.* **18**, 456–464 (2021).

49. Onufriev, M. V., Moiseeva, Y. V., Zhanina, M. Y., Lazareva, N. A. & Gulyaeva, N. V. A comparative study of Koizumi and Longa methods of intraluminal filament middle cerebral artery occlusion in rats: early corticosterone and inflammatory response in the hippocampus and frontal cortex. *Int. J. Mol. Sci.* https://doi.org/10.3390/ijms222413544 (2021).

50. Wang, Z. et al. The crosstalk signals of Sodium Tanshinone IIA Sulfonate in rats with cerebral ischemic stroke: Insights from proteomics. *Biomed. Pharmacother.* **151**, 113059 (2022).

51. Nguyen, J. N. et al. CD13 facilitates immune cell migration and aggravates acute injury but promotes chronic post-stroke recovery. *J. Neuroinflammation* **20**, 232 (2023).

Acknowledgements

Author contributions

Y.L., L.B.N., L.F. and J.F. have given substantial contributions to the conception and design of the manuscript, D.Z. and X.X.Z. to the acquisition, analysis, and interpretation of the data. All authors have participated in drafting the manuscript, and X.X.Z. and L.B.N. revised it critically. All authors read and approved the final version of the manuscript.

Competing interests

The authors declare no competing interests.

Additional information

Supplementary information The online version contains supplementary material available at https://doi.org/10.1038/s42003-024-07251-w.

Correspondence and requests for materials should be addressed to Xinxing Zhang, Lu Feng or Jing Fu.

Peer review information *Communications Biology* thanks the anonymous reviewers for their contribution to the peer review of this work. Primary Handling Editors: Toshiro Moroishi and Benjamin Bessieres.

Reprints and permissions information is available at http://www.nature.com/reprints

Publisher's note Springer Nature remains neutral with regard to jurisdictional claims in published maps and institutional affiliations.